Acta Biomaterialia 94 (2019) 524–535

Contents lists available at ScienceDirect

Acta Biomaterialia

journal homepage: www.elsevier.com/locate/actabiomat

Full length article

A computational multi-scale approach to investigate mechanically-induced changes in tricuspid valve anterior leaflet microstructure

Vineet S. Thomas [a], Victor Lai [b], Rouzbeh Amini [a,*]

[a] Department of Biomedical Engineering, The University of Akron, Akron, OH, United States
[b] Department of Chemical Engineering, University of Minnesota Duluth, Duluth, MN, United States

ARTICLE INFO

Article history:
Received 7 September 2018
Received in revised form 10 May 2019
Accepted 16 May 2019
Available online 20 June 2019

Keywords:
Collagen
Extracellular matrix
Finite element
Mechanobiology
Non-affine deformation
Representative volume element

ABSTRACT

The tricuspid valve is an atrioventricular valve that prevents blood backflow from the right ventricle into the right atrium during ventricular contractions. It is important to study mechanically induced microstructural alterations in the tricuspid valve leaflets, as this aids both in understanding valvular diseases and in the development of new engineered tissue replacements. The structure and composition of the extracellular matrix (ECM) fiber networks are closely tied to an overall biomechanical function of the tricuspid valve. In this study, we conducted experiments and implemented a multiscale modeling approach to predict ECM microstructural changes to tissue-level mechanical responses in a controlled loading environment. In particular, we characterized a sample of a porcine anterior leaflet at a macroscale using a biaxial mechanical testing method. We then generated a three-dimensional finite element model, to which computational representations of corresponding fiber networks were incorporated based on properties of the microstructural architecture obtained from small angle light scattering. Using five different biaxial boundary conditions, we performed iterative simulations to obtain model parameters with an overall R^2 value of 0.93. We observed that mechanical loading could markedly alter the underlying ECM architecture. For example, a relatively isotropic fiber network (with an anisotropy index value α of 28%) became noticeably more anisotropic (with an α of 40%) when it underwent mechanical loading. We also observed that the mechanical strain was distributed in a different manner at the ECM/fiber level as compared to the tissue level. The approach presented in this study has the potential to be implemented in pathophysiologically altered biomechanical and structural conditions and to bring insights into the mechanobiology of the tricuspid valve.

Statement of Significance

Quantifying abnormal cellar/ECM-level deformation of tricuspid valve leaflets subjected to a modified loading environment is of great importance, as it is believed to be linked to valvular remodeling responses. For example, developing surgical procedures or engineered tissue replacements that maintain/mimic ECM-level mechanical homeostasis could lead to more durable outcomes. To quantify leaflet deformation, we built a multiscale framework encompassing the contributions of disorganized ECM components and organized fibers, which can predict the behavior of the tricuspid valve leaflets under physiological loading conditions both at the tissue level and at the ECM level. In addition to future in-depth studies of tricuspid valve pathologies, our model can be used to characterize tissues in other valves of the heart.

1. Introduction

The tricuspid valve is one of the four valves in the heart. It regulates blood flow from the right atrium (RA)[1] to the right ventricle (RV). The tricuspid valve complex consists of three leaflets

* Corresponding author.
E-mail addresses: vst2@zips.uakron.edu (V.S. Thomas), laix0066@d.umn.edu (V. Lai), ramini@uakron.edu (R. Amini).

[1] All abbreviations are listed in the Table 2 of the Appendix.

https://doi.org/10.1016/j.actbio.2019.05.074
1742-7061/

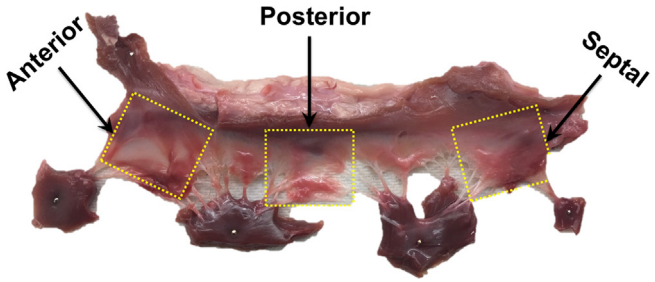

Fig. 1. Tricuspid valve excised from a porcine heart showing the anterior, posterior and the septal leaflets.

(i.e., anterior, posterior and septal leaflets), the annulus, and the chordae tendineae. The coordinated actions of the tricuspid valve components allow the three leaflets to coapt during the systolic phase and seal the passage between the RA and RV, directing blood to the lungs and preventing backflow into the RA.

The macroscopic and microscopic structure of the tricuspid valve is broadly classified within the tricuspid valve complex [1]. The tricuspid valve has three leaflets of different shapes and sizes (Fig. 1) that are attached to the annulus. They are transparent and thin; in contrast to the aortic and pulmonary valves, they cannot be readily separated into individual leaflets. The tricuspid valve leaflet microstructure is composed of fibrous skeleton and an endocardial surface. The anterior leaflet is the largest leaflet; it stretches from the funnel-shaped area downward to the inferior lateral wall of the right ventricle. The smallest leaflet is the posterior leaflet, which is attached to the tricuspid ring along its posterior inferior border. The septal leaflet is situated near the median plane of the tricuspid valve; it is attached to the muscular part of the ventricular septum and is supported by several chordae tendinae. The annulus of the tricuspid valve has a fibrous, well-defined cartilage-like structure in some areas and undergoes dynamic deformations during the cardiac cycle [2–4]. The chordae tendinae are composed of collagen fibrils that collectively form fiber bundles, which are arranged along the longitudinal axis of the chordae. Any disruption to the coordinated action of these components in the tricuspid valve complex results in tricuspid valve dysfunction (regurgitation or stenosis).

The mechanical integrity of the tricuspid valve leaflets relies on the underlining reinforcement of collagen fibers and other extracellular matrix (ECM) components. ECM collagen fiber networks have a major influence on the biomechanics of soft tissues including the tricuspid valve [5]. When surgical interventions are performed on the tricuspid valve, primarily to restore normal valve hemodynamics, the prevailing mechanical loading environment of the valve is modified. Among the few studies on the operative and overall mortality of patients post-TV surgeries, a study on 81 patients that was conducted between 1985 and 1999 [6] indicated that a high percentage of patients required re-operations accompanied by further cardiac procedures. From 1999 to 2008, approximately 150,000 patients have undergone TV repair surgeries in the United States [7]. According to the Society of Thoracic Surgery Database, in terms of morbidity and mortality, TV surgery remains the valve operation with the highest risk [8]. Approximately 1.6 million people in the United States suffer from TV regurgitation, which raises the number of potential candidates for TV repair [8–10]. Induced changes in the loading environment of the tricuspid valve due to repair surgeries may alter the ECM structure and composition over time [11]. Thus, it is necessary to clearly identify the link between the ECM microstructural architecture, microscale biomechanics, and the macroscale mechanical responses of the tricuspid valve leaflets. Such knowledge of multiscale tricuspid valve biomechanics is necessary to predict the response of the tricuspid valve when subjected to a modified loading environment resulting from tricuspid valve repair surgeries or other prevailing valve pathologies.

While previous studies have addressed the biomechanical behavior and complex geometry of the mitral valve (MV) and the aortic valve, the behavior and geometry of the tricuspid valve, which was once considered the forgotten valve, has not been studied thoroughly [12]. However, the tricuspid valve has received more attention in recent years due to efforts to increase the long-term survival of patients who undergo tricuspid valve surgeries. A follow-up survey revealed that even when normal tricuspid valve function was restored immediately after surgery, some patients developed mild, moderate and severe tricuspid valve regurgitation within five years [13]. Previous in vivo studies on the mitral valve showed that surgery affected the macroscale biomechanics of the valve [14]. Such induced changes in the macroscale biomechanics result in modifications in structure and microscale mechanics [15]. Computational models are effective tools to obtain insights into the biomechanical changes in the valve following surgery. At the current time, two computational models of the tricuspid valve have been mentioned in the literature [16,17]; however, the scope of these models is limited, as they are constructed based on homogenous mechanical properties. Without a microstructurally and mechanically accurate model of the tricuspid valve, it is difficult to conduct hypothesis-driven studies of valve pathologies, develop better surgical procedures, or improve treatment strategies.

Over the years, phenomenological constitutive models have been formulated that assume isotropic, linear/non-linear [18–21] and orthotropic or transversely-isotropic [22–29] material properties to define the response of tissues. However, the deformation of the tissue at ECM/cellular levels cannot be captured in these roughly approximated models, as the models did not consider the complex interactions of tissue components [30–33]. In an attempt to bridge this gap, a few investigators developed structurally based constitutive models that consider the ECM architecture of the tissue [34–41]. These models have been applied to other soft tissues such as those in the lungs, myocardium, and walls of the urinary bladder. In addition, a few man-made materials (e.g. elastomeric tissue scaffolds) have been studied using these structurally based models [42]. Although such microstructurally based models provide much more detail when compared to phenomenological models, they are limited by the assumption that ECM fibers affinely follow the macroscale (tissue-level) deformation [43]. For example, if at a point on the macro level, the tissue is stretched 10% in one direction, the same 10% stretch should be applied to the ECM at the micro-level. In other words, the independent rotation and extension of the fibers within the RVE (non-affine deformation) does not exist in these models. In most of the physiologically relevant cases, however, tissue deformations are not fully affine [44,45], and such models do not represent the accurate response of the tissue. However, the non-affinity of deformation specific to cardiac valves remains to be established.

The mechanical behavior of the cardiac valves at various length scales is currently a subject of wide interest. A multiscale approach for such structural constitutive models can provide valuable insights into the normal and abnormal functioning of cardiac valves [42,46,47]. Currently, no structurally based models are able to predict the behavior of the tricuspid valve. Our modeling approach allows for a more physiologically accurate representation of the tissue extra-cellular matrix, i.e. the non-affine deformation of the collagen fibers. Our modeling approach is consistent with the earlier experimental findings in other heart valves of noticeable changes in the orientation of collagen fibers under mechanical loading [48–50] and predicts the changes in the micro-environment under tissue-level loading. In this study, for the first time, we develop a framework to capture the complex biomechanical interactions in the tricuspid valve at different length scales.

2. Materials and methods

2.1. Macroscale characterization

Fresh porcine hearts were acquired from a local slaughterhouse (3-D Meats, Dalton, Ohio) and immediately transferred to our lab in a cold isotonic phosphate buffer saline (PBS) solution. As soon as the hearts arrived at the lab, the tricuspid valve leaflets were carefully excised from each heart and temporarily placed in specimen dishes containing PBS. A square-shaped sample (Fig. 2a) of the tricuspid valve anterior leaflet was extracted using a specially designed phantom [51]. The sample was then carefully mounted onto the biaxial testing equipment (Fig. 2b) using fish hooks as described by Amini-Khoiy et al. [51]. Ten cycles of equibiaxial loading were applied as preconditioning before the data were recorded. Each axis was loaded to 100 N/m and unloaded for approximately 20s after applying a tare load of 0.5 g. The load verses displacement data (Fig. 2c) was recorded at the end of the tenth cycle. In this study we consider loading the sample up to 40 N/m which corresponds to normal physiological pressure.

2.2. Microscale characterization

Once the data were obtained, the sample was carefully unmounted from the biaxial testing equipment. It was then rinsed thoroughly and mounted on a small angle light scattering (SALS) device (Fig. 2e) [52]. An in-house MATLAB code was used to control SALS equipment. A step size of 0.25 mm × 0.25 mm was chosen for our SALS analysis and a single image was obtained. Details about our custom-made SALS setup are provided in our recent publication [50]. Briefly, a random polarized 5 mW He-Ne laser beam (Model 1125) passing through the sample is scattered by the fibrous structures. The scattering pattern, which is projected on a Mylar screen, is digitized using a digital camera (Grasshopper3 2.3MP Mono USB3 Vision, GS3-U3-23S6M-C) installed behind the screen. Since the scattering pattern is perpendicular to the fiber direction θ, each fiber bundle contributes its scattered light intensity at an angle of $\theta + 90^{\circ}$. Fig. 2d shows the post-processed SALS scan output of a tricuspid valve anterior leaflet sample with the contour of anisotropy index α and mean fiber direction μ [50]. These network parameters were computed using a second-order orientation tensor H (Eq. (1)) [53,54]. In particular, the eigenvalues (λ_1, λ_2) and eigenvectors (V_1, V_2) of H were used to calculate the anisotropy index α (Eq. (2)) and the mean fiber direction μ (Eq. (3)).

$$H = \oint r \otimes r\, R(\theta) d\theta \tag{1}$$

$$\alpha = 100\left(1 - \frac{\lambda_1}{\lambda_2}\right) \quad where \quad \lambda_1 \leqslant \lambda_2 \tag{2}$$

$$\mu = tan^{-1}\left(\frac{V_2.j}{V_2.i}\right) \tag{3}$$

In Eq. (1), the symbol $\otimes$ represents the dyadic multiplication, r is a unit vector in the direction of θ (i.e., $r = [cos\theta\ sin\theta]$), and $R(\theta)$ represents the fiber network distribution. An anisotropy index value close to 100% indicates a well-oriented fiber network, whereas an index value close to 0% indicates a randomly oriented fiber network.

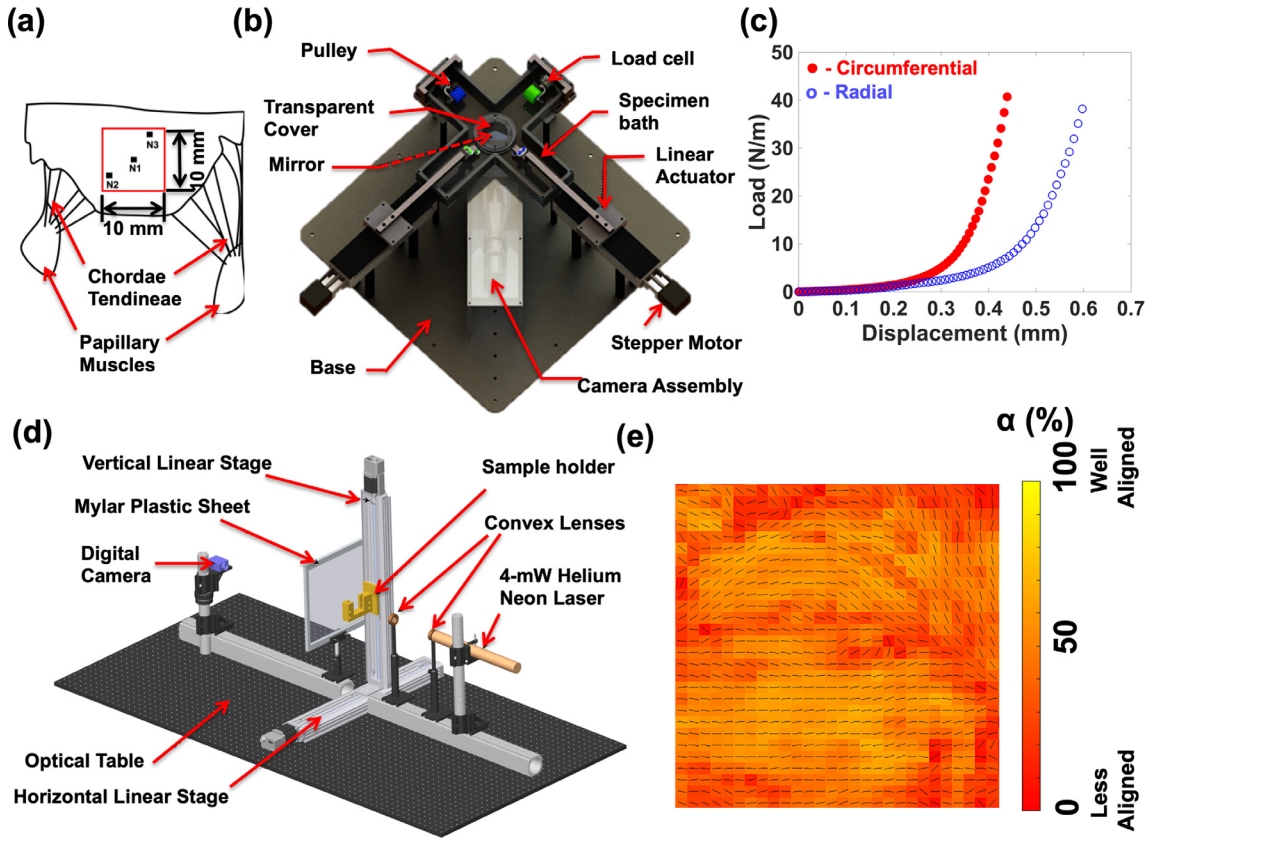

Fig. 2. (a) Schematic diagram of the tricuspid valve anterior leaflet marked with the sample extracted using a specially designed phantom [51]. (b) Schematic diagram of our custom made biaxial testing equipment [51]. (c) Equibiaxial tension test response of the sample in the circumferential (solid) and radial (hollow) directions. (d) Schematic diagram of the setup for small angle light scattering (SALS). (e) A contour map obtained for the anterior leaflet sample using SALS [50], showing the anisotropy index (α) contour and the mean fiber direction (μ) calculated based on Eqs. (1)–(3). Warmer colors indicate a more organized network. (For interpretation of the references to colour in this figure legend, the reader is referred to the web version of this article.)

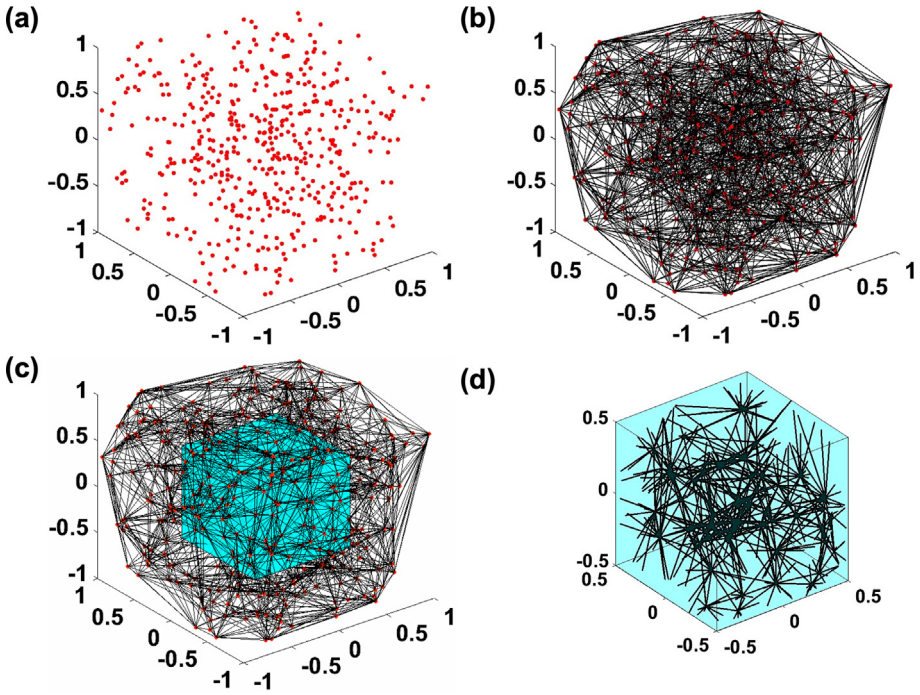

Fig. 3. (a) Random points generated between −1 and 1. (b) Delaunay triangulation algorithm applied to generate fibers. (c) Unit domain (1 × 1 × 1) chosen from the central region. (d) Representative volume element (RVE).

2.3. Generating three-dimensional representative volume elements

An internally-developed MATLAB program (based on the method described previously by Sander et al. [55] and Dhume et al. [56]) was used to generate 3D fiber networks to match the 2D measurements obtained using SALS. Random points were generated in three-dimensional (3D) space between −1 and 1 (Fig. 3a). Using the Delaunay triangulation algorithm, we identified three unique points to form a triangle whose edges were treated as fibers (Fig. 3b). A unit domain (1 × 1 × 1) was then clipped from the central region (Fig. 3c), which represents the fibrous component of the ECM (the solid line segments in Fig. 3c), and non-collagenous part of the ECM (the shaded region in Fig. 3d). The clipped domain was used as representative volume element (RVE). Since the points were chosen randomly at the initial steps, these types of RVEs were equivalent to a randomly oriented fibrous network. However, to generate a network with fibers aligned in any specific direction, the initial network was stretched and rotated with specific values prior to the clipping step. A library of network files having the desired α and μ when the fibers are projected on a two-dimensional plane (similar to projection of the fibers in SALS) were subsequently generated by adjusting the amount of stretch in the fibers and rotating them accordingly. The required networks were chosen from the library and were assigned to their corresponding finite elements according to the SALS measurement.

2.4. Description of the multi-scale model

The backbone of a multi-scale model initially developed to analyze collagen gels [47] was employed in this study. This model is designed at the macroscale and the microscale, representing the functional aspect and the structural aspect of the tissue, respectively. The three main assumptions of the model [47,57,58] are as follows:

1. The non-collagenous ECM and collagen fiber network are independent, and their stresses are additive.
2. The non-collagenous ECM is modeled as a compressible neo-Hookean material at the macroscale [59–61]. The Poisson ratio is set to 0.49 for modeling a nearly incompressible material.
3. The ECM collagen fiber–fiber interaction at the microscale is used to determine the mechanical response of the fiber network.

Separate RVEs are arranged at each of the eight Gauss points for every element in the finite element (FE) model. A schematic of the model arrangement is shown in Fig. 4, where the macroscale deformations are mapped to deformations of microscale RVE boundaries [57]. The RVE network rearranges and deforms in response to the RVE boundary deformations, which generates a macroscopic volume-averaged Cauchy stress S'_{ij} in terms of microscopic stress tensor s'_{ij} at each integration point within each FE as in Nemat-Nasser and Hori [62].

$$S'_{ij} = \frac{1}{V'} \int_V s'_{ij} dV \tag{4}$$

Further, on applying Green's theorem and assuming microscopic equilibrium (i.e. $s'_{ij,i} = 0$), Eq. (4) in its discrete form is given by Eq. (5), where the prime denotes dimensional quantity.

$$S'_{ij} = \frac{1}{V'} \sum_{boundary\ \ crosslinks} x'_i f_j \tag{5}$$

Since an undeformed RVE represents a computational space of a unit length, it is dimensionless. Dimensionless quantities are scaled and converted to dimensional quantities (i.e., $V' = \gamma V$ and $x'_i = \gamma x_i$, which are described in more detail in Table 3 in the Appendix) to represent a physical space in the tissue. The parameter γ represents the RVE edge length at the tissue level and, consequently, the total fiber length at the tissue level is γL. The fiber volume is computed as $\gamma L A_f$, in which A_f is the cross-sectional area of the fiber. The volume fraction ψ is, then, given by Eq. (6):

$$\psi = \frac{L A_f}{\gamma^2} \tag{6}$$

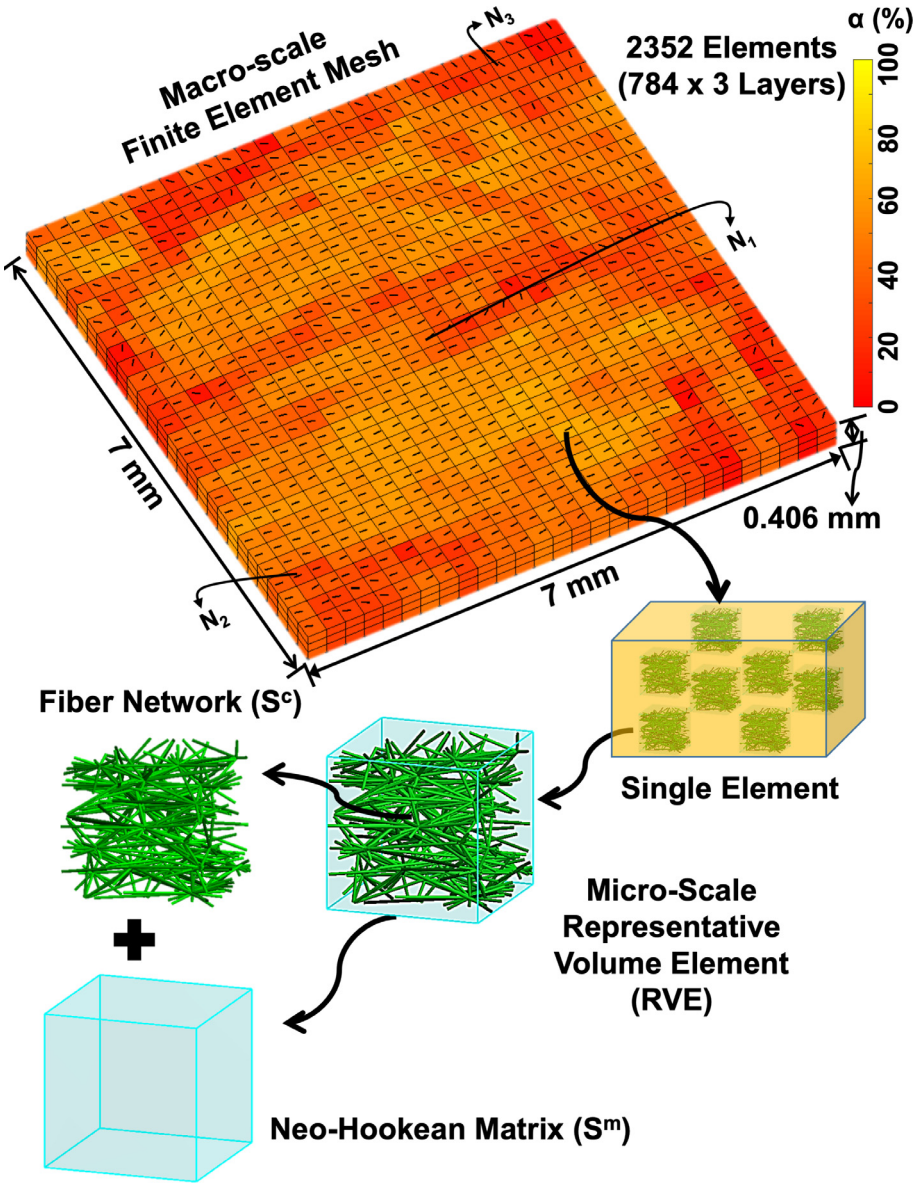

Fig. 4. Schematic diagram showing the arrangement of the multiscale finite element model.

which can be rewritten as Eq. (7)

$$\gamma = \sqrt{\frac{LA_f}{\psi}} \tag{7}$$

Substituting the scaled quantities in Eq. (5), the macroscopic RVE volume averaged Cauchy stress tensor S_{ij}^c is computed as in Chandran and Barocas (Eq. (8)) [47].

$$S_{ij}^c = \frac{\psi}{LA_f}\frac{1}{V}\sum_{boundary\ \ crosslinks} x_i f_j \tag{8}$$

A balance between the stress generated and the macroscale deformation is then obtained in an iterative manner [58]. The fibers are modeled as nonlinear springs with force f in the fibers governed by a nonlinear constitutive equation from Billiar and Sacks (Eq. (9)) [63], as long as the fiber stretch λ_f is less than a critical stretch value of λ_c. Beyond the critical stretch value of λ_c, the fiber forces are considered to change linearly with fiber stretch λ_f:

$$f = \begin{cases} \frac{E_f A_f}{\beta}\left(e^{\beta\varepsilon_G} - 1\right), & \lambda_f < \lambda_c \\ \frac{E_f A_f}{\beta}\left(e^{\beta\varepsilon_G^c} - 1\right) + E_f A_f \lambda_c e^{\beta\varepsilon_G^c}\left(\lambda_f - \lambda_c\right), & \lambda_f > \lambda_c \end{cases} \tag{9}$$

where $\varepsilon_G = \frac{1}{2}\left(\lambda_f^2 - 1\right)$ is the Green strain of the fiber and ε_G^c denotes the strain value corresponding to the critical stretch value λ_c.

The stress contribution from the non-collagenous matrix S_{ij}^m is computed using a neo-Hookean model from Bonet and Wood (Eq. (10)) [64].

$$S_{ij}^m = \frac{G}{J}\left(B_{ij} - \delta_{ij}\right) + \frac{2Gv}{J(1-2v)} ln(J)\delta_{ij} \tag{10}$$

where G is the shear modulus, B is the left Cauchy–Green deformation gradient tensor, and J is the determinant of the deformation gradient tensor F. Consistent with previous studies [65], the symbol v is used as a material constant that within the range of linear elasticity will be identical to the Poisson's ratio. As shown previously, such use of the Possion's ratio as a material parameter in the undeformed configuration allows the assumption of nearly incompressible material behavior for the values of v close to 0.5 [46,67–69]. It is worth noting that in generalized hyperelastic theory, the Possion's ratio is a function of stretch [71,71], which was not considered in our study. The stress contribution from the non-collagenous matrix is assumed to vary only on the macroscopic scale. Microscopic equilibrium

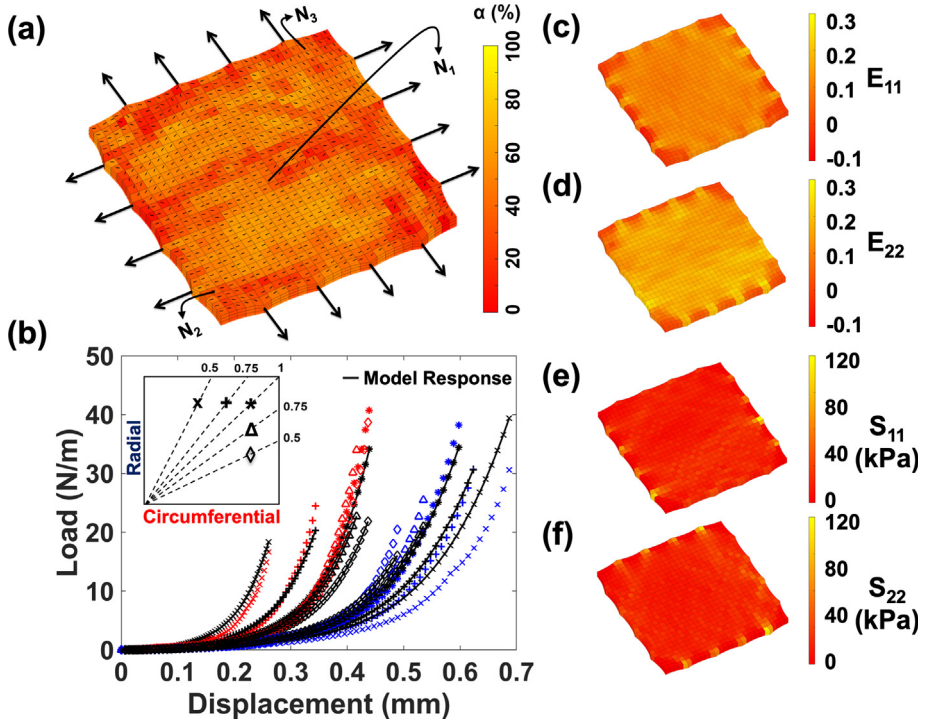

Fig. 5. (a) Deformed configuration of the FE model under equibiaxial loading conditions. (b) Simulated multiscale model response after fitting the model parameters to five loading protocols represented on the top left corner of the plot (circumferential: radial – 0.5:1 (×), 0.75:1 (+), 1:1 (∗), 1:0.75 (Δ), 1:0.5 (◇)) measured using biaxial tensile testing equipment ($R^2 = 0.93$). Deformed configuration of FE model with contours of green strain components (c) E_{11} & (d) E_{22} and Cauchy stress components (e) S_{11} & (f) S_{22}.

($s^c_{ij,i} = 0$) is assumed, and the Leibnitz theorem is applied to derive Eq. (11) for the divergence of the macroscopic stress tensor, where the right-hand side of Eq. (11) results from the pairing of the non-uniform stress and non-uniform deformation of the RVE boundary as described in detail in Chandran and Barocas [47].

$$S^c_{ij,i} + S^m_{ij,i} = \frac{1}{V}\oint_{\partial V}\left(s^c_{ij} - S^c_{ij}\right)u_{k,i}n_k dS \tag{11}$$

To solve the macroscopic boundary value problem with the applied boundary conditions, the deformation of the RVE boundaries is first determined by the macroscopic deformation field. The fiber force balance is then solved for each RVE. The volume-averaged Cauchy stress for the ECM fibers are calculated; it is then substituted into a macroscopic stress balance and solved iteratively. The Newton-Raphson method is used to iterate the nonlinear macroscopic FE problem and microscopic force balance until the solution converges. More details about this modeling approach are available in the literature [46,47,54,57,72,73].

2.5. Macroscale finite element model specification

A 3D finite element model of the anterior leaflet sample (7 mm × 7 mm × 0.406 mm) was developed and meshed with 2352 elements in three layers along its thickness (Fig. 4). An average of 450 fibers was maintained while generating RVEs for all elements, based on the microstructural parameters (anisotropy index α and mean fiber direction μ) obtained using the SALS equipment [52–54]. The networks generated were arranged in the model as shown in the schematic diagram in Fig. 4. The collagen fiber diameter and fiber volume fraction for our simulations were assumed to be 450 nm [74] and 43% [76,76], respectively. Five boundary conditions were simulated based on the five protocols (0.5:1, 0.75:1, 1:1, 1:0.75 and 1:0.5) test data. For each specific value of applied tension, the corresponding actuator displacements recorded during the experiment were used as the displacement boundary conditions on their respective edges of the model. The finite element model was simulated using a trial set of fitting parameters (shear modulus G, fiber modulus E_f, fiber critical stretch threshold λ_c, and parameter β to control the nonlinearity of the response), and the model response was validated using five protocols biaxial test data. Based on the model response in both the circumferential and the radial direction, changes to the four parameters were made, and the model was simulated again with the modified set of fitting parameters. This process was repeated until the measure for fitting quality R^2 approached 1.

Each RVE has ∼450 fibers, which equates to nearly 2700 degrees of freedom, leading to more than 50 million degrees of freedom for our FE model with 2352 elements. To expedite the

Table 1
[Minimum, maximum] strain (E_{11} & E_{22}) and [minimum, maximum] stress (S_{11} & S_{22}) components in the final deformed configuration of the FE model for the simulated five loading protocols.

Loading Protocols	E_{11}	E_{22}	S_{11} (kPa)	S_{22} (kPa)
0.5:1	[−0.0667, 0.1240]	[0.0024, 0.2433]	[−0.1108, 27.8545]	[−0.0636, 75.3780]
0.75:1	[−0.0452, 0.1514]	[0.0022, 0.2505]	[−0.1230, 53.3879]	[−0.0760, 90.0844]
1:1	[−0.0522, 0.2072]	[0.0022, 0.2594]	[−0.1379, 117.9156]	[−0.0902, 110.0844]
1:0.75	[−0.0522, 0.2239]	[0.0023, 0.2616]	[−0.1420, 141.7450]	[−0.0934, 115.3076]
1:0.5	[−0.0643, 0.2744]	[−0.0141, 0.2684]	[−0.1539, 221.9012]	[−0.1019, 130.3874]

solving process, the code was parallelized using the message passing interface (MPI) technique and submitted the Ohio Supercomputer Center (OSC) to run on its Ruby Cluster (which uses 200 2.6-GHz Intel Xeon E5-2670 processors) [77]. Typically, each simulation required a clock time of ~15 h to complete.

2.6. Statistical method

To evaluate the quality of fit between the model and the experimental data, we computed the coefficient of determination (R^2) [78]. The R^2 value was defined using Eq. (12):

$$R^2 = 1 - \frac{\sum_{i=1}^{n}(y_i - \hat{y}_i)^2}{\sum_{i=1}^{n}(y_i - \bar{y})^2} \tag{12}$$

where y_i refers to the experimental data, $\bar{y}$ is the mean of y_i and $\hat{y}_i$ refers to the values obtained from the simulation.

3. Results

Fig. 5a shows the deformed profile of the FE model in the final step of an equibiaxial tension test simulation. The multiscale model fitted all five loading protocols (0.5:1 [R^2 = 0.82], 0.75:1

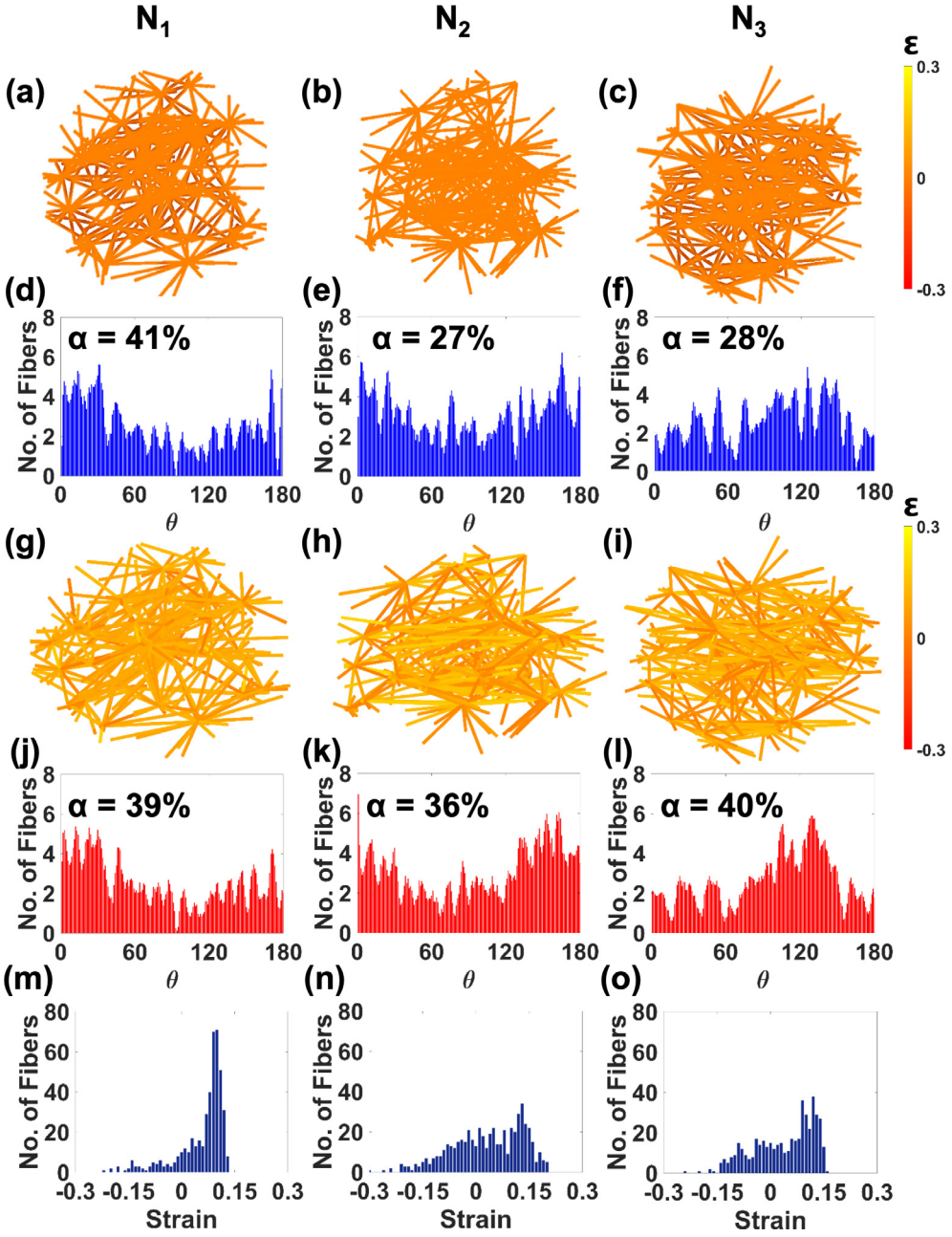

Fig. 6. Initial configuration of fiber networks chosen from (a) the belly region (N_1 in Fig. 4), (b) a location close to the left boundary (N_2 in Fig. 4), and (c) a location close to the top boundary (N_3 in Fig. 4). The fiber distribution histograms of the selected network at the undeformed configuration showing that (d) N_1 ($\alpha = 41\%$) had more organized network as compared to (e) N_2 ($\alpha = 27\%$) and (f) N_3 ($\alpha = 28\%$). The final deformed configurations of fiber networks (g) N_1, (h) N_2 and (i) N_3, with fibers under higher strain values shown in lighter colors. The fiber distribution histograms of deformed configurations showing that fiber orientation of (j) N_1 changes very little as compared to the larger changes in (k) N_2 and (l) N_3. Distribution of fiber strains (ε) at the final deformed configuration show that the majority of fibers in (m) N_1 had similar strain, whereas fibers in (n) N_2 and (o) N_3 experienced larger range of strains. (For interpretation of the references to colour in this figure legend, the reader is referred to the web version of this article.)

[R^2 = 0.99], 1:1 [R^2 = 0.98], 1:0.75 [R^2 = 0.93] and 1:0.5 [R^2 = 0.85]) with an overall R^2 value of 0.93 for the tricuspid valve anterior leaflet sample (Fig. 5b). While in situ loading for the most part was close to equibiaxial response (based on the assumption of law of Laplace), three loading protocols 0.75:1, 1:1 and 1:0.75 were considered for which, the model response fitted the data set with a R^2 value of 0.97. The R^2 obtained was on par with phenomenological models [25,63,26]. The model fit parameters for the anterior leaflet sample were as follows: G = 2.1 kPa, E_f = 10.5 kPa, β = 50.5 and λ_c = 1.12. The contour maps for Green strain (E_{11} & E_{22}) and Cauchy stress (S_{11} & S_{22}) components were shown in Fig. 5(c,d) and (e,f), respectively. Table 1 lists the minimum and maximum macroscale strain and stress components for each of the five simulated loading scenarios.

To demonstrate changes in the response of the ECM microstructure to macroscale equibiaxial loading as predicted by our multiscale model, three representative networks were chosen at different locations on the model as shown in Fig. 4: N_1, from a location in the belly region (Fig. 6a); N_2, from a location close to the left boundary (Fig. 6b); and N_3, from a location close to the top boundary (Fig. 6c). The color contour of true strain in the fiber was plotted; it shows that the initial strain for all fibers in the undeformed configuration is zero. The measure of fiber spread (i.e. the anisotropy index) in the undeformed networks were 41% for N_1 (Fig. 6d), 27% for N_2 (Fig. 6e), and 28% for N_3 (Fig. 6f). Fiber networks at the end of the simulated deformation are shown in Fig. 6(g–i). The fiber networks were found to have translated and rotated based on the RVE boundary deformation, and they realigned primarily in the direction of the applied load. The network N_1 in Fig. 6j did not show a prominent change in its alignment compared to its initial state. In contrast, networks N_2 (Fig. 6k) and N_3 (Fig. 6l) showed higher anisotropy index values after deformation, indicating that these networks became more aligned. The majority of fibers in network N_1 underwent strain values of approximately 13% (Fig. 6m). However, networks N_2 and N_3 showed a relatively even distribution of fibers up to a maximum strain of $\sim$ 30% (Fig. 6(n,o).

Fig. 7 shows the distribution of maximum principle strain E_1 in 2352 finite elements. The majority of elements in the FE model underwent strain levels below 20%. Fig. 7 also shows the distribution of fiber level strains using one-eighth of the fiber-containing RVEs in the model. To generate this distribution histogram, one RVE per FE was selected, and the fiber strain data were augmented in a master fiber strain data file. The reason for choosing only one RVE per element (instead of using all eight RVEs in each FE) was the limitation in storing a large number of data files at the high performance computer center. The fiber strain histogram shows that the majority of fibers underwent less than 20% strain, and only a small number of fibers had strain values between 20% and 30%. This complied with our fitted threshold fiber stretch value of 1.12 ($\sim$13% Green strain) which was less than 20% strain. Direct comparison of maximum principle strain E_1 and fiber strain is perhaps not an ideal method. Nevertheless, the two strains (one representing the macroscale and the other representing the microscale) were distributed in a noticeably different manner.

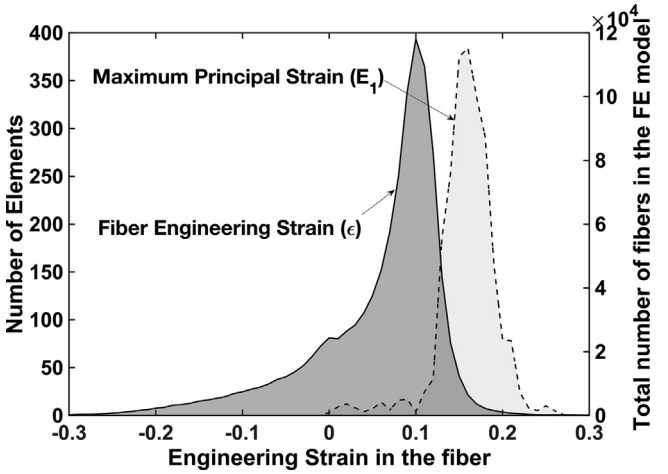

Fig. 7. Distribution of the maximum principal strain E_1 in the macroscale FE elements (light shaded region bounded with dotted line) and distribution of engineering strain ε in the fibers in all the elements (dark shaded region bounded with solid line).

4. Discussion

Using our multiscale approach, for the first time, it is possible to estimate changes in the ECM microstructural architecture of the tricuspid valve anterior leaflet in a controlled loading environment (Fig. 6). For example, when comparing the final deformed configuration (Fig. 5) with the undeformed configuration (Fig. 4), we observed slight changes in the anisotropy index contour in the central region of the model. However, towards the boundaries, we noticed more prominent changes in the anisotropy index with deformation (Fig. 5). One could assume that the central region was under in-plane biaxial deformation, whereas regions close to boundaries underwent non-biaxial deformations. Such differences could also be noticed by examining individual RVEs at different locations in the model. For instance, networks N_2 and N_3 (highlighted in Fig. 4) had similar anisotropy indices in the undeformed configuration (Fig. 6(b,c). For N_2, located close to the left boundary of the model, the anisotropy index increased from 27% to 36% (Fig. 6k). For N_3, the anisotropy index increased from 28% to 40% (Fig. 6l). Since tricuspid valve leaflets undergo complex deformations under more physiologically relevant conditions [79], our model can be used to predict ECM-level microstructural changes that are more relevant to the valvular mechanical environment. It is worth noting that our current SALS experimental measurements are limited, as we were not able to examine changes in the structural architecture of the *same* specimen under controlled biaxial deformation. We have recently conducted experiments showing that, on an average, the anisotropy index of the tricuspid valve anterior leaflet increases when it undergoes deformation due to an increase in the right ventricular pressure [50]. Future experimental measurements of ECM microstructural changes under controlled biaxial experiments using SALS or polarized light microscopy [54] can be used to quantitatively validate our results. Another emerging method to image ECM collagen fiber is second harmonic generation (SHG) microscopy, which is highly sensitive to changes in the collagen fiber structure due to its fundamental physical origin [80]. Fata et al. [81] were able to measure collagen recruitment under real-time deformations during biaxial tests using SHG microscopy. Therefore, such imaging techniques could aid in validating the microstructural response of our model.

We also observed that the mechanical strains between the ECM fibers of the tricuspid valve anterior leaflet are distributed differently than the strains in macroscale tissue. It is important to quantify the ECM-level strains, especially in the field of mechanobiology. Heart valves experience a dynamic mechanical environment due to the nature of their functions during each cardiac cycle. As such, one would expect that the ECM fibers undergo a range of homeostatic strains during their normal functions. Deviations from such homeostatic strains, whether they are caused by pathological lesions (such as chordae rupture [82]) and/or surgical interventions (such as ring annuloplasty [83]), could lead to changes in the mechanical integrity of the valve leaflets via damage and/or remodeling responses.

Increased levels of strains in soft tissues can lead to tissue damage, and previous studies have shown that ECM-level strains could predict such tissue damage under excessive mechanical loading [58]. Interestingly, the valvular ECM remodeling response is initiated due to both increased and decreased mechanical stresses, and decreased stress could lead to ECM degradation and a subsequent loss of structural integrity of the valve. Cardiac valves are known to contain molecules that control and regulate collagen degradation. In all types of cardiac valves, matrix metalloproteinase 1 (MMP-1) has been found [84]. In the tricuspid valve in particular, tissue inhibitors of metalloproteinases (TIMP-1, TIMP-2, and TIMP-3) are also present in the tissue and are believed to be synthesized by valve interstitial cells [85,85]. It is interesting that the mechanical environment directly affects enzymatic degradation of the ECM collagen. Experimental studies have shown that ECM collagen is more stable and degrades more slowly under homeostatic mechanical strain. In particular, Zareian and colleagues have shown that 1.5% mechanical strain decreases enzymatic activity by 50% and consequently delays rapid native ECM collagen degradation [86]. Flynn et al. [87] also investigated the concept of strain-dependent collagen degradation in a microbioreactor under controlled environment in which rearranged type I collagen micro-networks were strained gently between micropipettes [87]. A notable increase in the degradation time of loaded fibrils exposed to active MMP-8 was observed with applied mechanical tensile strain. These studies collectively show that the mechanical strains at the ECM level have a protective role and without some minimum level of strain, the ECM collagen degrades more rapidly. Although no study has been conducted on the tricuspid valve leaflets in particular, it is well known that many soft tissues have rate-dependent viscoelastic responses [89,89]. In fact, a recent study [90] has shown that a 1000-fold change in the strain rate can lead to different mechanical behavior in semilunar valve samples under biaxial loading. Notwithstanding the importance of this study, heart valves generally function within a narrow range of frequency (∼50–∼200 beats per minutes). While frequency is not the only paramter that can affect strain rates, as consistent with previous investigations [92,92], we used a quasi-static approach in the simulation of tricuspid valve leaflets. The current version of our model framework is not applicable for the simulation of viscoelastic materials that undergo a wide range of strain rates.

Considering the biomechanically induced remodeling responses of the ECM demonstrated in the above mentioned studies, it is not surprising that reducing fiber-level strains in the cardiac valves from their homeostatic levels would lead to changes in the ECM integrity. For example, Stephens et al. [93] have shown that making a surgical hole in the mitral valve leaflets in order to initiate regurgitation (and consequently changing the mechanical loads applied on the leaflets) would alter their ECM collagen content. However, without multiscale methods similar to the one developed in this study, it will not be possible to quantify the amount of change in the ECM-level strain values. The lack of such information precludes quantitative analysis of strain-dependent tissue remodeling. As stated above, macroscale changes in the tricuspid valve mechanical environment may occur due to many primary lesions (such as chordae rupture [82]), secondary diseases (such as pulmonary hypertension [94]), or surgical interventions (such as ring annuloplasty [83]). Such changes could directly affect collagen synthesis/degradation and subsequently affect the integrity of the valve and its normal function. The interdependence between ECM-level changes of strains/microstructure and the macroscale mechanical environment of the tricuspid valves in response to surgical procedures is a topic of active research in our laboratory.

We compared the fitted parameters of the tricuspid valve anterior leaflet with those obtained for other tissues (e.g., arterial wall, aorta, blood vessels, collagen gels, etc.) using similar multi-scale models [46,47,57,58,66,95]. We noticed that the values for the critical stretch (λ_c) and shear modulus (G) were similar to those of other tissues. However, values for the non-linear parameter β, which ranged from 0.25 to 10 in the studies with similar models, were smaller than our fitted β value of 50.5. The fiber modulus (E_f) parameter in the above mentioned studies was 2–3 orders of magnitude larger (ranging from 1.3 MPa to 43.2 MPa) than our fitted fiber modulus parameter. While our model was the first one developed using volume-averaging theory for the multi-scale responses of any cardiac valves, others have used the exponential fiber constitutive equations in modeling of the aortic valve leaflets using a top-to-bottom affine approach [63]. In particular, Billiar and Sacks used a similar exponential equation (formulated based on tension rather than stress) and found a wide range of values: between 0.0042 N/m and 0.16 N/m for the counterpart of the fiber modulus parameter in their model for glutaraldehyde-treated native aortic valves [63]. In the realm of phenomenological models, parameters for a non-linear Fung-type model of porcine tricuspid valve leaflets also covered a wide range of values between 0.4 kPa and 6.1 kPa [25]. Similarly, fitting non-linear models for carotid arteries under biaxial loading before and after exposure to elastase enzyme led to a wide range of parameter values with a high standard deviation in both groups [96]. Clearly, the non-linear nature of the constitutive models could be a reason for such wide range of fitted parameters. Since the primary focus of this study was development of a modeling framework for the tricuspid valve, a single sample (10 mm × 10 mm × 0.406 mm) extracted from the belly region of the tricuspid valve anterior leaflet was considered. Further analysis incorporating a larger number of samples of the tricuspid valve leaflets is necessary to identify a range of parameter values that can be used in future sensitivity studies [97].

To examine the uniqueness of the obtained model parameters, a sensitivity analysis was conducted by perturbing each of the four model fitting parameters by ±5% and keeping the other three parameters unchanged. Perturbing parameters by −5% and +5% resulted in percentage changes in the sum of the squared error (SSE) of 160.28% and 325.42% for λ_c, 35.66% and 39.74% for G, 36.94% and 42.82% for E_f, and 143.36% and 69.30% for β relative to the SSE computed for the model predicted response in Fig. 5. While it is necessary to conduct a more rigorous sensitivity analysis in the future, the increase in the SSE values after perturbing the parameters provides some level of confidence in the uniqueness of the obtained model parameters within the proximity of every single parameter domain. Further perturbation of the parameters and examination of the concavity of the error space can strengthen the fidelity of the specific fitted parameters for this sample [100,99]. Such perturbation analyses, however, are computationally costly due to the large size of the multi-scale model.

Our study is not without limitations. In our model, we have broadly classified the tissue sample into a fibrous component representing collagen and a non-fibrous component representing the remaining non-collagenous portion of the ECM and cells. This assumption was motivated by the fact that collagen is the main load-bearing component of the valve. However, classifying the fibrous part of the ECM into collagen and elastin can further improve our model. The addition of elastin fibers as a new fiber family will introduce three additional fitting parameters (elastin fiber modulus E_f^e, elastin fiber critical stretch threshold λ_c^e and a parameter β^e that controls the nonlinearity of the response for elastin fibers) into our model. Further, in this step of model development, we used porcine heart valve samples, which have been used in many other valvular biomechanical studies [100]. However, caution should be taken when drawing conclusions regarding human tissues from porcine studies. For example, a previous study

comparing the biomechanical properties and microstructure of aged human and healthy porcine aortic valve leaflets showed significant differences in both the mechanical (human valve leaflets are less compliant) and structural aspects (human valve leaflets contained more collagen and elastin) of the tissues of the two species [101].

5. Conclusions

The computational multiscale finite element model implemented in our study is capable of capturing the mechanical response of the tricuspid valve anterior leaflet. This model provides insight into changes in the tricuspid valve ECM microstructural architecture and fiber strains due to an altered mechanical loading environment. It has the potential to predict remodeling responses in pathophysiological conditions that affect the mechanical loading of the tricuspid valve, similar to remodeling response models developed for other biological materials [102].

Acknowledgement

Funding for this project was provided in part by American Heart Association Grant No. 16SDG27770088. Computing resources were provided by the Ohio Supercomputer Center in Columbus, Ohio. The authors would like to thank Victor H. Barocas for sharing the source code for the multi-scale FE solver used in the development of this study. The thoughtful comments of Sheila Pearson are acknowledged, as is the assistance from Vahhab Zarei, Mohammad F. Hadi, and Julia Quindlen in conducting this study. The educational material is based upon work supported by the National Science Foundation under NSF CAREER Award No. 1846715.

Appendix A

As part of our commitment to broadening the impact of our research work, we have developed an educational component related to the research work presented in this manuscript. In this Appendix, we have provided a "homework assignment" that is appropriate for a graduate-level introductory course in biomechanics or continuum mechanics.

Problem – As discussed in the method section, the stress in the non-collagenous matrix S_{ij} was computed using a neo-Hookean model from Bonet and Wood (Eq. (13)) [64].

$$S_{ij} = \frac{G}{J}\left(B_{ij} - \delta_{ij}\right) + \frac{2Gv}{J(1-2v)}\ln(J)\delta_{ij} \tag{13}$$

We also stated that the use of the Possion's ratio as a material parameter in the undeformed configuration in this formulation allows the assumption of nearly incompressible material behavior for the values of v close to 0.5. As shown by Bonet and Wood [64], within the range of small strains, the standard fourth order elasticity tensor can be recovered from Eq. (13). In such a case, the assumption that $v \to \frac{1}{2}$ leads to incompressibilty is easy to prove. The purpose of this exercise, however, is to show that even for large strains, the specific form of the constitutive relation presented in Eq. (13) guarantees that as $v \to \frac{1}{2}$, the volume has to stay constant and, thus, the material behavior becomes nearly incompressible. To demonstrate such a response, you may start from any arbitrary deformation gradient tensor F_{ij} that is expressed in terms of its eigenvalues λ_i in a coordinate system (Eq. (14)), which aligns with its orthogonal eigenvectors:

$$\mathbf{F} = \begin{bmatrix} \lambda_1 & 0 & 0 \\ 0 & \lambda_2 & 0 \\ 0 & 0 & \lambda_3 \end{bmatrix} \tag{14}$$

Table 2
Abbreviations used in this document.

Abbreviation	Full form
3D	Three-dimensional
ECM	Extracellular matrix
FE	Finite element
MPI	Message passing interface
MV	Mitral valve
PBS	Phosphate buffer saline
MMP	Matrix metalloproteinase
RA	Right atrium
RV	Right ventricle
RVE	Representative volume element
SALS	Small angle light scattering
TIMP	Tissue inhibitor of metalloproteinases
SHG	Second harmonic generation
SSE	Sum of the squared error

Table 3
List of model parameters.

Model Parameter	Description
ψ	Fiber volume fraction
γ	RVE edge length
L	Dimensionless length of the fibers
A_f	Fiber cross sectional area
V	RVE volume
x_i	Position of the boundary cross-link
f_j	Force generated at the fiber level
ε_G	Fiber Green strain
ϵ_G^c	Green strain at threshold fiber stretch
E_f	Fiber modulus
λ_f	Fiber longitudinal stretch ratio
λ_c	Fiber critical stretch threshold
β	Exponential parameter representing the non-linearity of the force response
G	Shear modulus
μ	Poisson's ratio
J	Determinant of the deformation gradient tensor F ($F_{ij} = \frac{\partial x_i}{\partial X_j}$)
B_{ij}	Left Cauchy–Green deformation tensor ($B_{ij} = F_{ik}F_{jk}$)
S_{ij}^c	Volume averaged Cauchy stress from collagenous matrix
S_{ij}^m	Stress contribution from non-collagen matrix
s_{ij}^c	Microscopic stress tensor from collagenous matrix
u_k	Displacement of the RVE boundary
n_k	Unit normal vector

In the first part of the problem, calculate the components of the left Cauchy–Green deformation tensor and subsequently use them to calculate the components of Cauchy stress. The Cauchy stress tensor should be in the following form (Eq. (15)):

$$\mathbf{S} = \begin{bmatrix} \frac{G}{J}\left[\lambda_1^2 - 1 + \frac{2v}{(1-2v)}\ln(J)\right] & 0 & 0 \\ 0 & \frac{G}{J}\left[\lambda_2^2 - 1 + \frac{2v}{(1-2v)}\ln(J)\right] & 0 \\ 0 & 0 & \frac{G}{J}\left[\lambda_3^2 - 1 + \frac{2v}{(1-2v)}\ln(J)\right] \end{bmatrix} \tag{15}$$

In the second part of the problem, show that as $v \to \frac{1}{2}$, the only acceptable finite deformation is the one in which $ln\ (J) \to 0$, i.e., $J \to 1$ and, thus, the material behavior has to be incompressible.

References

[1] M. Misfeld, H.-H. Sievers, Heart valve macro-and microstructure, Philos. Trans. R. Soc. B: Biol. Sci. 362 (1484) (2007) 1421–1436.
[2] M.K. Rausch, M. Malinowski, P. Wilton, A. Khaghani, T.A. Timek, Engineering analysis of tricuspid annular dynamics in the beating ovine heart, Ann. Biomed. Eng. 46 (3) (2018) 443–451.
[3] M.K. Rausch, M. Malinowski, W.D. Meador, P. Wilton, A. Khaghani, T.A. Timek, The effect of acute pulmonary hypertension on tricuspid annular height, strain, and curvature in sheep, Cardiovasc. Eng. Technol. (2018) 1–12.
[4] H. Fawzy, K. Fukamachi, C.D. Mazer, A. Harrington, D. Latter, D. Bonneau, L. Errett, Complete mapping of the tricuspid valve apparatus using three-dimensional sonomicrometry, J. Thoracic Cardiovasc. Surg. 141 (4) (2011) 1037–1043.
[5] Y.-C. Fung, Biomechanics: Mechanical Properties of Living Tissues, Springer Science & Business Media, 2013.
[6] P.M. McCarthy, S.K. Bhudia, J. Rajeswaran, K.J. Hoercher, B.W. Lytle, D.M. Cosgrove, E.H. Blackstone, Tricuspid valve repair: durability and risk factors for failure, J. Thoracic Cardiovasc. Surg. 127 (3) (2004) 674–685.
[7] C.M. Vassileva, J. Shabosky, T. Boley, S. Markwell, S. Hazelrigg, Tricuspid valve surgery: the past 10 years from the nationwide inpatient sample (nis) database, J. Thoracic Cardiovasc. Surg. 143 (5) (2012) 1043–1049.
[8] A. Kilic, P. Saha-Chaudhuri, J.S. Rankin, J.V. Conte, Trends and outcomes of tricuspid valve surgery in north america: an analysis of more than 50,000 patients from the society of thoracic surgeons database, Ann. Thoracic Surg. 96 (5) (2013) 1546–1552.
[9] J.P. Singh, J.C. Evans, D. Levy, M.G. Larson, L.A. Freed, D.L. Fuller, B. Lehman, E.J. Benjamin, Prevalence and clinical determinants of mitral, tricuspid, and aortic regurgitation (the framingham heart study), Am. J. Cardiol. 83 (6) (1999) 897–902.
[10] O. Stuge, J. Liddicoat, Emerging opportunities for cardiac surgeons within structural heart disease, J. Thoracic Cardiovasc. Surg. 132 (6) (2006) 1258–1261.
[11] S.F. Badylak, D.O. Freytes, T.W. Gilbert, Extracellular matrix as a biological scaffold material: structure and function, Acta Biomater. 5 (1) (2009) 1–13.
[12] P.M. McCarthy, V.L. Sales, Evolving indications for tricuspid valve surgery, Curr. Treatment Options Cardiovasc. Med. 12 (6) (2010) 587–597.
[13] Z.-W. Ge, Z.-Y. Cheng, B.-C. Wang, J.-L. Hu, J.-C. Li, Z.-N. Zhao, G. Qiao, X.-Q. Quan, G.-B. Zhang, et al., Clinical efficacy of two different tricuspid annuloplasty techniques in left cardiac valve surgery, Asian Pacific J. Trop. Med. 11 (2) (2018) 166.
[14] R. Amini, C.E. Eckert, K. Koomalsingh, J. McGarvey, M. Minakawa, J.H. Gorman, R.C. Gorman, M.S. Sacks, On the in vivo deformation of the mitral valve anterior leaflet: effects of annular geometry and referential configuration, Ann. Biomed. Eng. 40 (7) (2012) 1455–1467.
[15] S. Cho, J. Irianto, D.E. Discher, Mechanosensing by the nucleus: from pathways to scaling relationships, J. Cell Biol. (2017). jcb–201610042.
[16] M. Stevanella, E. Votta, M. Lemma, C. Antona, A. Redaelli, Finite element modelling of the tricuspid valve: a preliminary study, Med. Eng. Phys. 32 (10) (2010) 1213–1223.
[17] F. Kong, T. Pham, C. Martin, R. McKay, C. Primiano, S. Hashim, S. Kodali, W. Sun, Finite element analysis of tricuspid valve deformation from multi-slice computed tomography images, Ann. Biomed. Eng. (2018) 1–16.
[18] M. Taramasso, H. Vanermen, F. Maisano, A. Guidotti, G. La Canna, O. Alfieri, The growing clinical importance of secondary tricuspid regurgitation, J. Am. Coll. Cardiol. 59 (8) (2012) 703–710.
[19] A. Cataloglu, R.E. Clark, P.L. Gould, Stress analysis of aortic valve leaflets with smoothed geometrical data, J. Biomech. 10 (3) (1977) 153–158.
[20] M.S. Hamid, H.N. Sabbah, P.D. Stein, Large-deformation analysis of aortic valve leaflets during diastole, Eng. Fract. Mech. 22 (5) (1985) 773–785.
[21] M. Black, I. Howard, X. Huang, E. Patterson, A three-dimensional analysis of a bioprosthetic heart valve, J. Biomech. 24 (9) (1991) 793–801.
[22] R. Haj-Ali, L.P. Dasi, H.-S. Kim, J. Choi, H. Leo, A.P. Yoganathan, Structural simulations of prosthetic tri-leaflet aortic heart valves, J. Biomech. 41 (7) (2008) 1510–1519.
[23] R.A. Boerboom, N.J. Driessen, C.V. Bouten, J.M. Huyghe, F.P. Baaijens, Finite element model of mechanically induced collagen fiber synthesis and degradation in the aortic valve, Ann. Biomed. Eng. 31 (9) (2003) 1040–1053.
[24] G. Burriesci, I. Howard, E. Patterson, Influence of anisotropy on the mechanical behaviour of bioprosthetic heart valves, J. Med. Eng. Technol. 23 (6) (1999) 203–215.
[25] K.A. Khoiy, A.D. Pant, R. Amini, Quantification of material constants for a phenomenological constitutive model of porcine tricuspid valve leaflets for simulation applications, J. Biomech. Eng. 140 (9) (2018) 094503.
[26] K.A. Khoiy, S. Abdulhai, I.C. Glenn, T.A. Ponsky, R. Amini, Anisotropic and nonlinear biaxial mechanical response of porcine small bowel mesentery, J. Mech. Behav. Biomed. Mater. 78 (2018) 154–163.
[27] G. Arcidiacono, A. Corvi, T. Severi, Functional analysis of bioprosthetic heart valves, J. Biomech. 38 (7) (2005) 1483–1490.
[28] H. Kim, J. Lu, M.S. Sacks, K.B. Chandran, Dynamic simulation pericardial bioprosthetic heart valve function, J. Biomech. Eng. 128 (5) (2006) 717–724.
[29] A. Smuts, D. Blaine, C. Scheffer, H. Weich, A. Doubell, K. Dellimore, Application of finite element analysis to the design of tissue leaflets for a percutaneous aortic valve, J. Mech. Behav. Biomed. Mater. 4 (1) (2011) 85–98.
[30] K.J. Grande, R.P. Cochran, P.G. Reinhall, K.S. Kunzelman, Stress variations in the human aortic root and valve: the role of anatomic asymmetry, Ann. Biomed. Eng. 26 (4) (1998) 534–545.
[31] N.J. Driessen, C.V. Bouten, F.P. Baaijens, A structural constitutive model for collagenous cardiovascular tissues incorporating the angular fiber distribution, J. Biomech. Eng. 127 (3) (2005) 494–503.
[32] H. Kim, K.B. Chandran, M.S. Sacks, J. Lu, An experimentally derived stress resultant shell model for heart valve dynamic simulations, Ann. Biomed. Eng. 35 (1) (2007) 30–44.
[33] H. Kim, J. Lu, M.S. Sacks, K.B. Chandran, Dynamic simulation of bioprosthetic heart valves using a stress resultant shell model, Ann. Biomed. Eng. 36 (2) (2008) 262–275.
[34] K. Li, W. Sun, Simulated thin pericardial bioprosthetic valve leaflet deformation under static pressure-only loading conditions: implications for percutaneous valves, Ann. Biomed. Eng. 38 (8) (2010) 2690–2701.
[35] Y. Lanir, Constitutive equations for fibrous connective tissues, J. Biomech. 16 (1) (1983) 1–12.
[36] G.A. Holzapfel, T.C. Gasser, R.W. Ogden, A new constitutive framework for arterial wall mechanics and a comparative study of material models, J. Elasticity Phys. Sci. Solids 61 (1–3) (2000) 1–48.
[37] R. Gnyaneshwar, R.K. Kumar, K.R. Balakrishnan, Dynamic analysis of the aortic valve using a finite element model, Ann. Thoracic Surg. 73 (4) (2002) 1122–1129.
[38] W. Sun, M.S. Sacks, Finite element implementation of a generalized fung-elastic constitutive model for planar soft tissues, Biomech. Model. Mechanobiol. 4 (2–3) (2005) 190–199.
[39] E.J. Weinberg, M.R. Kaazempur-Mofrad, A large-strain finite element formulation for biological tissues with application to mitral valve leaflet tissue mechanics, J. Biomech. 39 (8) (2006) 1557–1561.
[40] F. Migliavacca, R. Balossino, G. Pennati, G. Dubini, T.-Y. Hsia, M.R. de Leval, E.L. Bove, Multiscale modelling in biofluidynamics: application to reconstructive paediatric cardiac surgery, J. Biomech. 39 (6) (2006) 1010–1020.
[41] A. Saleeb, A. Kumar, V. Thomas, The important roles of tissue anisotropy and tissue-to-tissue contact on the dynamical behavior of a symmetric tri-leaflet valve during multiple cardiac pressure cycles, Med. Eng. Phys. 35 (1) (2013) 23–35.
[42] T. Courtney, M.S. Sacks, J. Stankus, J. Guan, W.R. Wagner, Design and analysis of tissue engineering scaffolds that mimic soft tissue mechanical anisotropy, Biomaterials 27 (19) (2006) 3631–3638.
[43] C.-H. Lee, P.J. Oomen, J.P. Rabbah, A. Yoganathan, R.C. Gorman, J.H. Gorman, R. Amini, M.S. Sacks, A high-fidelity and micro-anatomically accurate 3d finite element model for simulations of functional mitral valve, in: International Conference on Functional Imaging and Modeling of the Heart, Springer, 2013, pp. 416–424.
[44] P.L. Chandran, V.H. Barocas, Affine versus non-affine fibril kinematics in collagen networks: theoretical studies of network behavior, J. Biomech. Eng. 128 (2) (2006) 259–270.
[45] D. Hepworth, A. Steven-Fountain, D. Bruce, J. Vincent, Affine versus non-affine deformation in soft biological tissues, measured by the reorientation and stretching of collagen fibres through the thickness of compressed porcine skin, J. Biomech. 34 (3) (2001) 341–346.
[46] T. Stylianopoulos, V.H. Barocas, Multiscale, structure-based modeling for the elastic mechanical behavior of arterial walls, J. Biomech. Eng. 129 (4) (2007) 611–618.
[47] P.L. Chandran, V.H. Barocas, Deterministic material-based averaging theory model of collagen gel micromechanics, J. Biomech. Eng. 129 (2) (2007) 137–147.
[48] S.H. Alavi, A. Sinha, E. Steward, J.C. Milliken, A. Kheradvar, Load-dependent extracellular matrix organization in atrioventricular heart valves: differences and similarities, Am. J. Physiol.-Heart Circulatory Physiol. 309 (2) (2015) H276–H284.
[49] E.M. Joyce, J. Liao, F.J. Schoen, J.E. Mayer Jr, M.S. Sacks, Functional collagen fiber architecture of the pulmonary heart valve cusp, Ann. Thoracic Surg. 87 (4) (2009) 1240–1249.
[50] A.D. Pant, V.S. Thomas, A.L. Black, T. Verba, J.G. Lesicko, R. Amini, Pressure-induced microstructural changes in porcine tricuspid valve leaflets, Acta Biomater. 67 (2018) 248–258.
[51] K.A. Khoiy, R. Amini, On the biaxial mechanical response of porcine tricuspid valve leaflets, J. Biomech. Eng. 138 (10) (2016) 104504.
[52] M.S. Sacks, D.B. Smith, E.D. Hiester, A small angle light scattering device for planar connective tissue microstructural analysis, Ann. Biomed. Eng. 25 (4) (1997) 678–689.
[53] S.G. Advani, C.L. Tucker III, The use of tensors to describe and predict fiber orientation in short fiber composites, J. Rheol. 31 (8) (1987) 751–784.
[54] E.A. Sander, V.H. Barocas, Comparison of 2D fiber network orientation measurement methods, J. Biomed. Mater. Res. Part A 88 (2) (2009) 322–331.
[55] E.A. Sander, T. Stylianopoulos, R.T. Tranquillo, V.H. Barocas, Image-based biomechanics of collagen-based tissue equivalents, IEEE Eng. Med. Biol. Mag. 28 (3) (2009) 10–18.
[56] R.Y. Dhume, E.D. Shih, V.H. Barocas, Multiscale model of fatigue of collagen gels, Biomech. Model. Mechanobiol. (2018) 1–13.
[57] T. Stylianopoulos, V.H. Barocas, Volume-averaging theory for the study of the mechanics of collagen networks, Comput. Methods Appl. Mech. Eng. 196 (31–32) (2007) 2981–2990.

[58] M.F. Hadi, E.A. Sander, V.H. Barocas, Multiscale model predicts tissue-level failure from collagen fiber-level damage, J. Biomech. Eng. 134 (9) (2012) 091005.
[59] M.C. Wu, R. Zakerzadeh, D. Kamensky, J. Kiendl, M.S. Sacks, M.-C. Hsu, An anisotropic constitutive model for immersogeometric fluid–structure interaction analysis of bioprosthetic heart valves, J. Biomech. 74 (2018) 23–31.
[60] R. Avazmohammadi, D.S. Li, T. Leahy, E. Shih, J.S. Soares, J.H. Gorman, R.C. Gorman, M.S. Sacks, An integrated inverse model-experimental approach to determine soft tissue three-dimensional constitutive parameters: application to post-infarcted myocardium, Biomech. Model. Mechanobiol. 17 (1) (2018) 31–53.
[61] A. Drach, A.H. Khalighi, M.S. Sacks, A comprehensive pipeline for multi-resolution modeling of the mitral valve: validation, computational efficiency, and predictive capability, Int. J. Numer. Methods Biomed. Eng. 34 (2) (2018) e2921.
[62] S. Nemat-Nasser, M. Hori, Micromechanics: overall properties of heterogeneous materials, 37, Elsevier, 2013.
[63] K.L. Billiar, M.S. Sacks, Biaxial mechanical properties of the native and glutaraldehyde-treated aortic valve cusp: Part II: a structural constitutive model, J. Biomech. Eng. 122 (4) (2000) 327–335.
[64] J. Bonet, R.D. Wood, Nonlinear Continuum Mechanics for Finite Element Analysis, Cambridge University Press, 1997.
[65] T.J. Pence, K. Gou, On compressible versions of the incompressible neo-Hookean material, Math. Mech. Solids 20 (2) (2015) 157–182.
[66] S.B. Shah, C. Witzenburg, M.F. Hadi, H.P. Wagner, J.M. Goodrich, P.W. Alford, V.H. Barocas, Prefailure and failure mechanics of the porcine ascending thoracic aorta: experiments and a multiscale model, J. Biomech. Eng. 136 (2) (2014) 021028.
[67] S. Jouzdani, R. Amini, V.H. Barocas, Contribution of different anatomical and physiologic factors to iris contour and anterior chamber angle changes during pupil dilation: theoretical analysis, Invest. Ophthalmol. Visual Sci. 54 (4) (2013) 2977–2984.
[68] R. Amini, J.E. Whitcomb, M.K. Al-Qaisi, T. Akkin, S. Jouzdani, S. Dorairaj, T. Prata, E. Illitchev, J.M. Liebmann, R. Ritch, et al., The posterior location of the dilator muscle induces anterior iris bowing during dilation, even in the absence of pupillary block, Invest. Ophthalmol. Visual Sci. 53 (3) (2012) 1188–1194.
[69] A.D. Pant, L. Kagemann, J.S. Schuman, I.A. Sigal, R. Amini, An imaged-based inverse finite element method to determine in-vivo mechanical properties of the human trabecular meshwork, J. Model. Ophthalmol. 1 (3) (2017) 100.
[70] M.F. Beatty, D. Stalnaker, The Poisson function of finite elasticity, J. Appl. Mech. 53 (4) (1986) 807–813.
[71] N. Scott, The incremental bulk modulus, Young's modulus and Poisson's ratio in nonlinear isotropic elasticity: physically reasonable response, Math. Mech. Solids 12 (5) (2007) 526–542.
[72] J.C. Quindlen, V.K. Lai, V.H. Barocas, Multiscale mechanical model of the pacinian corpuscle shows depth and anisotropy contribute to the receptor's characteristic response to indentation, PLoS Comput. Biol. 11 (9) (2015) e1004370.
[73] T. Stylianopoulos, C.A. Bashur, A.S. Goldstein, S.A. Guelcher, V.H. Barocas, Computational predictions of the tensile properties of electrospun fibre meshes: effect of fibre diameter and fibre orientation, J. Mech. Behav. Biomed. Mater. 1 (4) (2008) 326–335.
[74] A. D'Amore, S.K. Luketich, G.M. Raffa, S. Olia, G. Menallo, A. Mazzola, F. D'Accardi, T. Grunberg, X. Gu, M. Pilato, et al., Heart valve scaffold fabrication: bioinspired control of macro-scale morphology, mechanics and micro-structure, Biomaterials 150 (2018) 25–37.
[75] C.M. Pierlot, A.D. Moeller, J.M. Lee, S.M. Wells, Pregnancy-induced remodeling of heart valves, Am. J. Physiol.-Heart Circulatory Physiol. 309 (9) (2015) H1565–H1578.
[76] B.V. Rego, M.S. Sacks, A functionally graded material model for the transmural stress distribution of the aortic valve leaflet, J. Biomech. 54 (2017) 88–95.
[77] O.S. Center, Ohio supercomputer center, URL:http://osc.edu/ark:/19495/f5s1ph73, 1987.
[78] J. Neter, M.H. Kutner, C.J. Nachtsheim, W. Wasserman, Applied Linear Statistical Models, vol. 4, Irwin Chicago, 1996.
[79] K.A. Khoiy, D. Biswas, T.N. Decker, K.T. Asgarian, F. Loth, R. Amini, Surface strains of porcine tricuspid valve septal leaflets measured in ex vivo beating hearts, J. Biomech. Eng. 138 (11) (2016) 111006.
[80] X. Chen, O. Nadiarynkh, S. Plotnikov, P.J. Campagnola, Second harmonic generation microscopy for quantitative analysis of collagen fibrillar structure, Nat. Protoc. 7 (4) (2012) 654.
[81] B. Fata, C.A. Carruthers, G. Gibson, S.C. Watkins, D. Gottlieb, J.E. Mayer, M.S. Sacks, Regional structural and biomechanical alterations of the ovine main pulmonary artery during postnatal growth, J. Biomech. Eng. 135 (2) (2013) 021022.
[82] V.K. Reddy, S. Nanda, N. Bandarupalli, K.R. Pothineni, N.C. Nanda, Traumatic tricuspid papillary muscle and chordae rupture: emerging role of three-dimensional echocardiography, Echocardiography 25 (6) (2008) 653–657.
[83] K. Matsuyama, M. Matsumoto, T. Sugita, J. Nishizawa, Y. Tokuda, T. Matsuo, Y. Ueda, De Vega annuloplasty and Carpentier-Edwards ring annuloplasty for secondary tricuspid regurgitation, J. Heart Valve Disease 10 (4) (2001) 520–524.
[84] A.C. Liu, V.R. Joag, A.I. Gotlieb, The emerging role of valve interstitial cell phenotypes in regulating heart valve pathobiology, Am. J. Pathol. 171 (5) (2007) 1407–1418.
[85] S. Dreger, P. Taylor, S. Allen, M. Yacoub, Profile and localization of matrix metalloproteinases (MMPs) and their tissue inhibitors (TIMPs) in human heart valves, J. Heart Valve Disease 11 (6) (2002) 875–880.
[86] R. Zareian, K.P. Church, N. Saeidi, B.P. Flynn, J.W. Beale, J.W. Ruberti, Probing collagen/enzyme mechanochemistry in native tissue with dynamic, enzyme-induced creep, Langmuir 26 (12) (2010) 9917–9926.
[87] B.P. Flynn, A.P. Bhole, N. Saeidi, M. Liles, C.A. DiMarzio, J.W. Ruberti, Mechanical strain stabilizes reconstituted collagen fibrils against enzymatic degradation by mammalian collagenase matrix metalloproteinase 8 (mmp-8), PLoS One 5 (8) (2010) e12337.
[88] E.D. Bell, M. Converse, H. Mao, G. Unnikrishnan, J. Reifman, K.L. Monson, Material properties of rat middle cerebral arteries at high strain rates, J. Biomech. Eng. 140 (7) (2018) 071004.
[89] A. Karunaratne, S. Li, A.M. Bull, Nano-scale mechanisms explain the stiffening and strengthening of ligament tissue with increasing strain rate, Scientific Rep. 8 (1) (2018) 3707.
[90] A. Anssari-Benam, Y.-T. Tseng, Gerhard A. Holzapfel, A. Bucchi, Rate-dependency of the mechanical behaviour of semilunar heart valves under biaxial deformation, Acta Biomater. 88 (10) (2019) 120–130. 1742-7061.
[91] J.S. Grashow, M.S. Sacks, J. Liao, A.P. Yoganathan, Planar biaxial creep and stress relaxation of the mitral valve anterior leaflet, Ann. Biomed. Eng. 34 (10) (2006) 1509–1518.
[92] J.S. Grashow, A.P. Yoganathan, M.S. Sacks, Biaixal stress–stretch behavior of the mitral valve anterior leaflet at physiologic strain rates, Ann. Biomed. Eng. 34 (2) (2006) 315–325.
[93] E.H. Stephens, T.C. Nguyen, A. Itoh, N.B. Ingels, D.C. Miller, K.J. Grande-Allen, The effects of mitral regurgitation alone are sufficient for leaflet remodeling, Circulation 118 (14 Suppl 1) (2008) S243–S249.
[94] E. Bossone, M. Rubenfire, D.S. Bach, M. Ricciardi, W.F. Armstrong, Range of tricuspid regurgitation velocity at rest and during exercise in normal adult men: implications for the diagnosis of pulmonary hypertension, J. Am. Coll. Cardiol. 33 (6) (1999) 1662–1666.
[95] E.A. Sander, T. Stylianopoulos, R.T. Tranquillo, V.H. Barocas, Image-based multiscale modeling predicts tissue-level and network-level fiber reorganization in stretched cell-compacted collagen gels, Proc. Natl. Acad. Sci. 106 (42) (2009) 17675–17680.
[96] J. Ferruzzi, M.J. Collins, A.T. Yeh, J.D. Humphrey, Mechanical assessment of elastin integrity in fibrillin-1-deficient carotid arteries: implications for Marfan syndrome, Cardiovasc. Res. 92 (2) (2011) 287–295.
[97] A. Voorhees, N.-J. Jan, I. Sigal, Effects of collagen microstructure and material properties on the deformation of the neural tissues of the lamina cribrosa, Acta Biomater. 58 (2017) 278–290.
[98] A.D. Pant, S.K. Dorairaj, R. Amini, Appropriate objective functions for quantifying iris mechanical properties using inverse finite element modeling, J. Biomech. Eng. 140 (7) (2018) 074502.
[99] A.D. Pant, P. Gogte, V. Pathak-Ray, S.K. Dorairaj, R. Amini, Increased iris stiffness in patients with a history of angle-closure glaucoma: an image-based inverse modeling analysis, Invest. Ophthalmol. Visual Sci. 59 (10) (2018) 4134–4142.
[100] M.S. Sacks, W.D. Merryman, D.E. Schmidt, On the biomechanics of heart valve function, J. Biomech. 42 (12) (2009) 1804–1824.
[101] C. Martin, W. Sun, Biomechanical characterization of aortic valve tissue in humans and common animal models, J. Biomed. Mater. Res. Part A 100 (6) (2012) 1591–1599.
[102] M. Hadi, E. Sander, J. Ruberti, V. Barocas, Simulated remodeling of loaded collagen networks via strain-dependent enzymatic degradation and constant-rate fiber growth, Mech. Mater. 44 (2012) 72–82.